

Falguni GORANA <sup>1</sup>, Yashwant Kumar MODI <sup>1</sup>

# Influence of build orientation on porosity, strength and dimensional accuracy of laser sintered polyamide porous bone scaffolds

Received 15 December 2023, Revised 9 April 2024, Accepted 25 April 2024, Published online 28 May 2024

**Keywords:** build orientation, compressive strength, impact strength, PA2200, porous bone scaffold, selective laser sintering

Development of synthetic bone graft via bone tissue engineering involves seeding of patient's stem cells onto a porous scaffold in presence of growth factors. Porosity, strength and dimensional accuracy of the porous scaffold play a vital role in this process. This work aims at ascertaining influence of build orientation on porosity, mechanical strength and dimensional accuracy of the selectively laser sintered polyamide porous scaffolds. Initially, CAD models of test specimens with pre-designed porosity were created in Solidworks® software. All the specimens were fabricated on EOSINT P395, a selective laser sintering machine, along various primary (Flat, Edge, Upright and Flat\_diag) and secondary (0°, 30°, 45°, 60° and 90°) orientations. Results show that measured porosity of most of the specimens was (range: 42.89–35.26%) less than the designed porosity (41.71%). Maximum average tensile strength (16.84 MPa) was recorded for specimens printed along Flat\_0° orientation. Specimens printed along Upright\_90° orientation showed highest average compressive strength (8.26 MPa). Specimens printed along Flat orientation showed relatively better average impact strength. Best dimensional accuracy was obtained for specimens printed along Flat orientation.

## 1. Introduction

Bone consists of two different structures, 1) a hard outer layer known as cortical bone and 2) a soft, spongy inner layer known as cancellous bone. This unique structure makes bone hard and strong yet light in weight. Bone is well known

✉ Yashwant Kumar MODI, e-mail: [yashwant.modi@juet.ac.in](mailto:yashwant.modi@juet.ac.in)

<sup>1</sup>Department of Mechanical Engineering, Jaypee University of Engineering and Technology, Guna, MP, India



© 2024, The Author(s). This is an open-access article distributed under the terms of the Creative Commons Attribution (CC-BY 4.0, <https://creativecommons.org/licenses/by/4.0/>), which permits use, distribution, and reproduction in any medium, provided that the author and source are cited.

for its excellent self-healing abilities. However, external intervention is usually needed to heal the critical-sized defect completely [1]. The external intervention mainly involves tissue-grafting and synthetic material replacement. Two tissue-grafting approaches, namely auto graft (bone taken from the patient's own body) and allograft (bone taken from a donor) are quite popular. However, tissue-grafting as well as synthetic material-replacement has certain limitations. Tissue grafting includes limitations such as donor-site morbidity, unavailability of adequate volume and quality of bone, non-availability of donor, infection and rejection by the host body. Synthetic materials do not show a perfect integration with host tissue and usually fail over a period due to wear and fatigue [2–5].

Bone tissue engineering (BTE), a sub-branch of tissue engineering, has emerged as one of the most promising approaches to repair critical-sized bone defects [5]. BTE involves development of implantable bone substitutes by seeding isolated cells onto a porous scaffold in presence of tissue-inducing substances. For successful regeneration of the bone, porous scaffold should be biocompatible, biodegradable, osteoconductive and osteoinductive. In addition, it must possess adequate compressive strength to withstand the pressure exerted by the sprouting cells [6–8]. Researchers developed several techniques such as freeze-drying, salt leaching, solvent casting, fibre bonding, electro spinning, gas foaming etc., to fabricate porous scaffold. However, these techniques do not offer any precise mechanism to control the shape and size of interconnected pores. Furthermore, customized shapes are also difficult to be produced [9, 10]. In order to overcome the aforementioned limitations, researchers started exploring additive manufacturing (AM) to fabricate porous scaffolds for BTE. Several researchers found AM to be very much capable of controlling not only the shape and size of the pores but also very efficient in producing custom-shaped scaffolds [11–14]. Researchers have explored different AM technologies, namely liquid resin based stereolithography, extrusion based fused deposition modelling, ceramic powder based inkjet 3D printing, powder bed based selective laser sintering as well as directed energy deposition based technologies for this purpose [15–18].

Selective laser sintering (SLS) is one of the most widely used AM technologies for fabricating polymer based porous scaffolds. SLS technology involves selective sintering of polyamide powder material spread onto a platform by using a laser beam. In comparison to stereolithography or fused deposition modelling, SLS does not require any support structure as the loose unfused powder spread onto the platform itself becomes support to the sintered portion. This reduces post processing time and cost. Polyamide (PA12) is a widely used polymer for SLS technology. It is a biocompatible material and suitable for bone scaffold [19]. Due to inherent additive nature of the SLS technology, certain amount of inconsistencies in size, shape, porosity and mechanical properties of the fabricated parts are likely to occur.

Several researchers tried establishing relationship between process parameters and properties of the produced parts by conducting various kinds of physical,

mechanical, and micro structural investigations [20–24]. Jain et al. (2008) [25] conducted experiments to evaluate tensile strength of PA2200 parts fabricated via SLS process and identified layer thickness, part bed temperature, hatch pattern and refresh rate as key parameters, which affect the part strength. Pilipovic et al. [26] studied effect of energy density on flexural strength of selective laser sintering parts. They varied energy densities by changing beam overlay at constant speed and power to conduct various experiments. They evaluated flexural properties at different density as well as the effect of beam overlay on density of the fabricated parts. Singh et al. [27] investigated compressive strength of polyamide (PA2200) scaffold structures useful in tissue engineering. They designed porous structures using computer-aided design (CAD) modelling software and fabricated on SLS system at different energy densities. Authors observed higher contribution of laser power, scan spacing, and layer thickness than scan speed on compressive strength of the fabricated scaffolds. Mousa [28] employed Taguchi design of experiment approach to investigate the effect of process parameters on the curling of the selective laser sintered specimens. The specimens were fabricated using composites of PA12 and PA12 mixed with a rigid multiphase-coated particle. They found layer thickness as the largest influencer for curling of the fabricated specimens. Other parameters like laser power, bed temperature and filler ratio had little contribution towards curling of the specimens.

Goodridge et al. [29] revealed through their investigation that selective laser sintering of polymer powder was influenced majorly by layer thickness, energy density, build orientation, build position, rate of cooling and type of powder (fresh or recycled). Mengqi et al. [30] investigated effects of orientation of three mutually perpendicular planes on the resolution of wedges and lithospheres geometries fabricated in PA12 material. The resolution was measured using stereomicroscopy for the mutually perpendicular planes. They observed better contrast and resolution for parts fabricated in vertical planes rather than horizontal plane. Guido et al. [31] conducted experiments on selective laser sintering, laser melting and fused deposition modelling processes for identifying the geometrical characteristics of additively manufactured parts. For selective laser sintering process, basic geometrical elements were fabricated using PA2200 polymeric material. After sample evaluation, authors reported the best possible orientations, directions, thicknesses and radius for different elements. Berti et al. [32] investigated mechanical properties of PA-Al<sub>2</sub>O<sub>3</sub> composite samples fabricated via selective laser sintering process. The samples were fabricated at different orientation angles in the build chamber. They observed a higher anisotropy in vertical direction of sintering. Moreover, higher influence of sintering direction was found with increasing temperature of the build chamber. Stoia et al. [33] conducted experiments to identify the influence of orientation on tensile strength of polyamide PA2200 samples fabricated through selective laser sintering process and observed best tensile properties for samples oriented at 0°.

Feng et al. [34] fabricated specimens at different orientations on FDM printer with polyamid-12 filament prepared using fresh and recycled powder material.

They studied effect of orientation on tensile, bending and impact strength of the specimens and concluded that specimens fabricated along  $x$ -axis with fresh powder were superior in terms of mechanical properties. Zárýbnická [35] investigated influence of additives and print orientations (along  $x$ -,  $y$ - and  $z$ -axis) on tensile strength, surface roughness and toughness of the PA-12 specimens fabricated on EOS's SLS system. A decrease in tensile strength and an increase in toughness and surface roughness of the printed samples were observed on inclusion of additives. Tensile strength of the samples printed along  $z$ -axis was found worst; whereas, along  $x$ - and  $y$ -axis, it was found quite similar and better than the  $z$ -axis. El Magri et al. [36], studied influence of laser power and hatch orientation on the tensile strength of the selective laser sintered PA12 parts. Results showed best tensile strength at highest laser power and at  $0^\circ$  orientation in XY plane.

It has been observed from literature review that orientation of part in build chamber play a significant role in deciding mechanical strength of the fabricated parts. Nevertheless, majority of the studies have been performed using solid specimens. Only a few studies reported consideration of porous specimens to conduct the mechanical tests. In the light of all the findings from the literature review, a good scope is realised for a comprehensive study that ascertains effect of important part build orientations via fabrication of porous specimens. This study aims to evaluate the influence of part orientation on measured porosity, mechanical properties and dimensional accuracy of the selective laser sintered PA2200 porous specimens mimicking the porous bone scaffolds.

## 2. Material and methods

### 2.1. Material

PA2200 powder, a proprietary material by EOS GmbH, Germany, was used to fabricate all the porous specimens in this study. It is a nylon based on polyamide-12. PA2200 is a semi-crystalline, white coloured, fine-grained polymer material with average grain size  $56 \mu\text{m}$ . It is a biocompatible (according to EN ISO 10993-1 and USP/level VI/ $121^\circ\text{C}$ ) material having a melting temperature range from  $172$ – $180^\circ\text{C}$ . The bulk density of the powder is  $450 \text{ kg/m}^3$  and density of laser-sintered part is  $930 \text{ kg/m}^3$ . Its ability to offer good strength, durability and heat resistance make it suitable for wide range of medical applications [37]. The powder used to carry out this study is a mixture of new and old (recycled) powder. The new and old powders were mixed in ratio of 30:70. The old powder was already recycled two times.

### 2.2. CAD Modelling of test specimens

It is a known fact that porosity of synthetic scaffolds should be enough to allow cell proliferation and nutrient flow. Pore size ranging from  $100$  to  $900 \mu\text{m}$  and porosity in range of  $30$ – $70\%$  were found suitable by researchers for cell attachment,

proliferation and nutrient flow through porous scaffolds [9, 38]. De-powdering of the hollow features has been an important consideration for powder bed printers. Authors of this paper via pilot study for PA2200 powder on EOSINT P395 m/c found 800  $\mu\text{m}$  to be the smallest pore size that can be de-powdered easily. So, considering all these facts, it was decided to keep the pore size approx. 800  $\mu\text{m}$  and porosity not less than 30% for the test specimens.

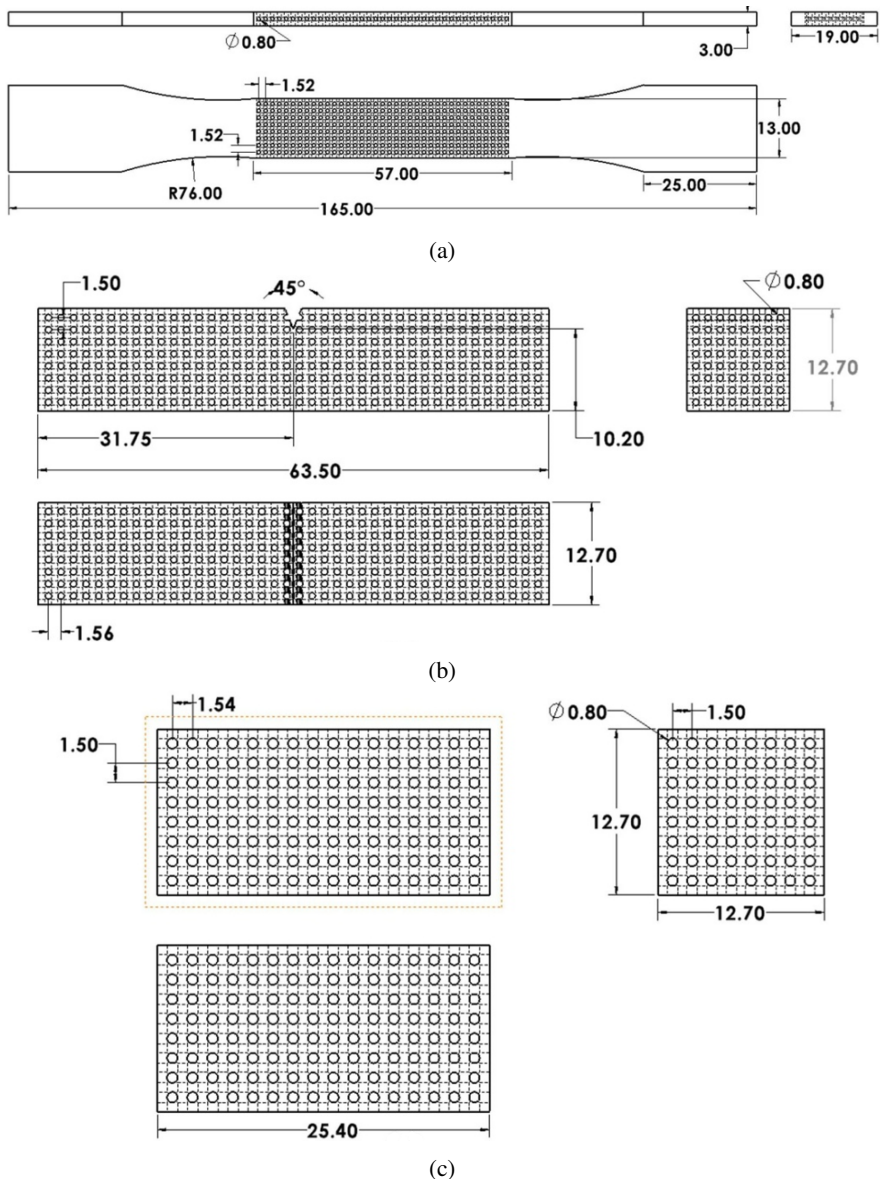


Fig. 1. Orthographic views of (a) tensile, (b) compression, and (c) impact (Izod) test specimens

CAD models of the porous specimens were created using Solidworks® software (Dassault Systems, France). Test specimens for tensile, compression and impact test were prepared according to ASTM D638, ASTM D695 and ASTM D256 standards respectively. The CAD models of tensile, compression and impact test (Izod) are shown in Fig. 1.

### 2.3. Additive manufacturing of test specimens

The prepared CAD models of the specimens were first saved into AM compatible .stl file format. It was important to choose .stl parameters carefully, so that minute details of the porous specimens could be maintained. The .stl file parameters for compression model were as follows: deviation tolerance: 0.01426996 mm, angle tolerance: 10°, number of triangles: 691564. The size of .stl file was 691564 MB.

Once all the CAD models were converted into .stl format, they were loaded into MagicsRP software for build preparation. In order to study the effect of part orientation in the build chamber, the specimens were kept in different orientations. The specimens were kept along four primary (Flat, Edge, Upright and Flat\_diag) and five secondary (0°, 30°, 45°, 60° and 90°) orientations in the build chamber as depicted in Fig. 2. Three copies of each CAD model were arranged in each orientation to avoid the fabrication as well as measurement errors.

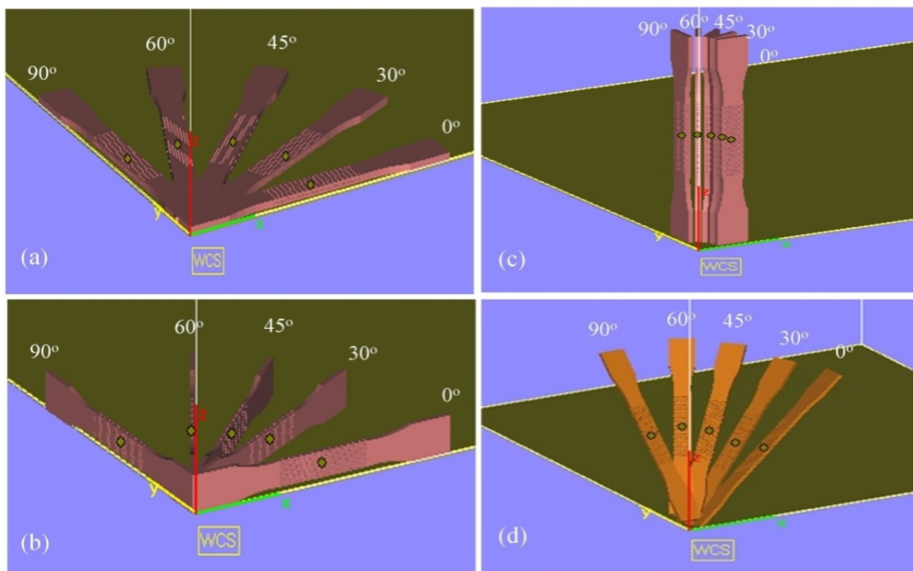


Fig. 2. Representation of primary (a) lat, (b) Edge, (c) Upright, and (d) Flat\_diag along with secondary orientations of specimens inside build chamber

After preparing the build volume, slicing of the models was performed using RP Tools software. Finally, sliced data was transferred to PSW 3.6 software of the EOSINT P395, a selective laser sintering machine by Electro Optical System (EOS)

Germany. All the specimens were fabricated at the following process parameters; laser type: CO<sub>2</sub>, laser power: 50 W, scan speed: 8 m/s, build temperature: 176°C and layer thickness: 0.12 mm. Initially, AM machine was kept on warm-up mode for 2 hours to bring the temperature inside the chamber to the desired level. After that, fabrication of specimen started in layer-by-layer manner. After fabrication, the machine was left idle for about 8–9 hours to cool down the chamber and avoid warpage and distortion of the fabricated specimens. Three specimens of each type were fabricated to enhance the repeatability and accuracy of results. Finally, all the specimens were removed from the build chamber. The image of specimen of each type is shown in Fig. 3.

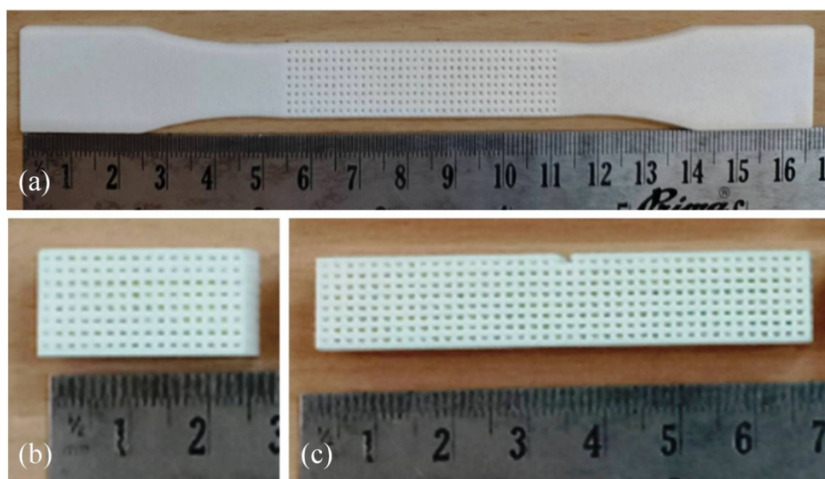


Fig. 3. Photographs of the fabricated specimens (a) tensile, (b) compression, and (c) impact

#### 2.4. Methods of measurement and testing

Particle size distribution of PA2200 powder was performed using a sieve shaker as well as Malvern particle size analyser. X-ray diffraction (XRD) of the powder material was carried out using Panalytical Empyrean XRD diffractometer. The scanning electron microscope (SEM) images were obtained through high-resolution field emission scanning electron microscope (ULTRA Plus, Zeiss). Macro porosity measurement was done using micro-CT scanning and reconstruction of 3D virtual model of the porous specimens. Mechanical performance of the fabricated specimens was assessed through tensile, compression and impact strength testing. A compression-testing machine, Tinius Olsen H5KL with 10 kN load-cell and a cross-head loading rate of 0.5 mm per minute was employed to measure the tensile and compressive strength of the fabricated prototypes. Tinius Olsen, IT 503 plastics impact tester was used to conduct the Izod impact test of the specimens. Digital Vernier calliper with least count 0.01 mm was used to measure the linear dimension of the fabricated specimens.

### 3. Results and discussions

#### 3.1. Material characterization

Particle size distribution (PSD) has significant effect on final quality of the selective laser sintered parts. Particles with diameter higher than  $40\ \mu\text{m}$  usually exhibit a good flowability. Smaller particles inhibit smooth flow due to sticky characteristics [39]. A sieve shaker consisting of a set of sieves ranging from 1700 to  $53\ \mu\text{m}$  mesh was used for the purpose and the result obtained is shown in Fig. 4.

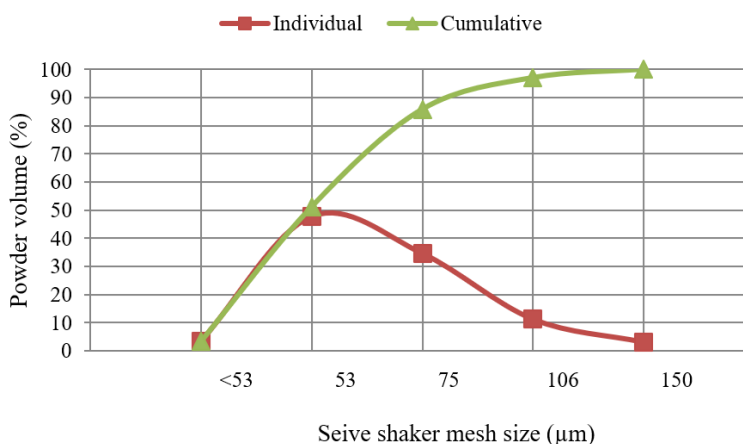


Fig. 4. Particle size distribution of PA2200 powder via sieve shaker

It can be observed that about 85% particles are below  $75\ \mu\text{m}$  and about 96% particles are smaller than  $106\ \mu\text{m}$ . Analysis on particle size analyser revealed that  $D_{10}$ ,  $D_{50}$  and  $D_{90}$  values were corresponding to  $33.7\ \mu\text{m}$ ,  $56.4\ \mu\text{m}$  and  $75.2\ \mu\text{m}$ , respectively. This means that 50% of the particles are equal or smaller than  $56.4\ \mu\text{m}$  and 90% particles are equal or smaller than  $75.2\ \mu\text{m}$ .

PA2200 powder consists of crystalline as well as amorphous region, making it a semi-crystalline polymer. It mainly exhibits two different crystal structures, namely the metastable  $\alpha$ -structure and the stable  $\gamma$ -crystalstructure. Fig. 5 shows x-ray diffraction pattern of the used PA2200 powder material. The XRD pattern mainly exhibits the metastable  $\alpha$ -phase, which has a molecular chain oriented in an anti-parallel manner with a high crystalline ratio [21, 22]. Diffraction peaks at the angle  $9.5^\circ$  and  $10^\circ$  show  $\alpha$ -crystal structure.

SEM images, shown in Fig. 6, were obtained using a high-resolution field emission scanning electron microscope (ULTRA Plus, Zeiss). Fig. 6a reveals that powder particles have spherical as well as irregular shapes. Surface of some of the particles has cracks also. This may be due to mixing of new with old powder. New particles are likely to be regular in shape. In Fig. 6b, we can see that shape of the hole is not perfectly circular, due to sticking of powder particles. This may be one

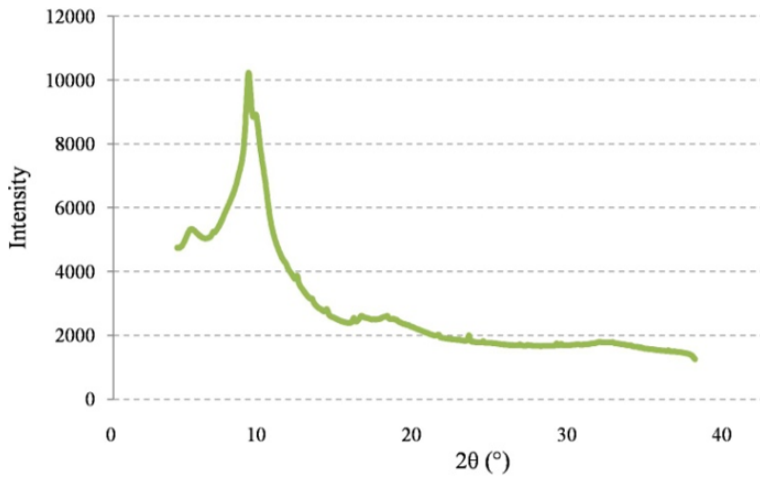


Fig. 5. XRD pattern of PA2200 powder

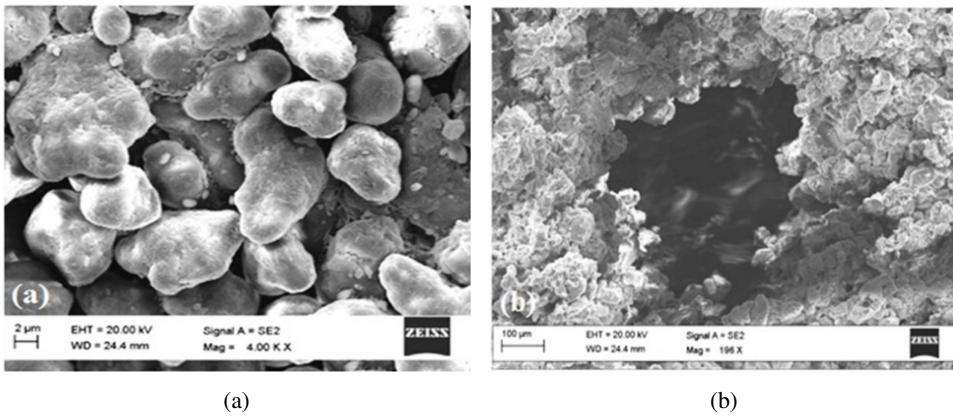


Fig. 6. SEM images of PA200 (a) powder, and (b) fabricated specimen

of the prominent reasons behind variation in the measured macro porosity from the designed porosity.

### 3.2. Macro porosity

The cuboid shaped (compression test) porous specimen, shown in Fig. 3b, was used to analyse the macro porosity of the fabricated specimens. The individual as well as average macro porosity of three specimens along with one standard deviation (SD), was computed and summarised in Table 1.

The designed porosity of the cuboid shaped specimen was calculated as 41.71% through Solidworks® software. Careful observation of Table 1 reveals that measured porosity is lower than the designed porosity for almost all the specimens printed along various orientations. The highest individual measured porosity ob-

Table 1. Individual and average measured porosity (%) for various orientations

Primary orientation	Specimen no.	Secondary orientation				
		0°	30°	45°	60°	90°
Flat	S1	40.7	40.58	39.85	39.42	41.68
	S2	41.9	39.82	39.55	40.26	41.36
	S3	40.22	40.13	38.46	38.57	42.89
	Avg±SD	40.94±0.87	40.18±0.38	39.29±0.73	39.42±0.85	41.98±0.81
Edge	S1	42.25	39.34	39.72	40.85	38.72
	S2	40.14	39.88	38.26	39.65	41.36
	S3	41.37	38.67	40.12	38.94	40.14
	Avg±SD	41.25±1.06	39.30±0.61	39.37±0.98	39.81±0.97	40.07±1.32
Upright	S1	39.72	39.72	37.42	38.53	38.78
	S2	39.68	37.28	36.58	35.66	39.36
	S3	38.08	39.36	38.25	39.78	39.18
	Avg±SD	40.16±0.94	38.79±1.32	37.42±0.84	37.99±2.11	39.11±0.30
Flat_diag	S1	36.47	37.78	38.45	38.84	38.2
	S2	38.56	35.26	35.42	37.68	36.06
	S3	36.88	38.75	35.77	36.14	37.82
	Avg±SD	37.30±1.11	37.26±1.80	36.55±1.66	37.55±1.35	37.36±1.14

tained is 42.89% for specimen printed along Flat<sub>90°</sub> orientation; whereas, the lowest porosity obtained is 35.26% for specimen printed along Flat<sub>diag</sub><sub>30°</sub> orientation.

To visualise and compare the results in a better and easy way, average measured porosity for various orientations is depicted in Fig. 7.

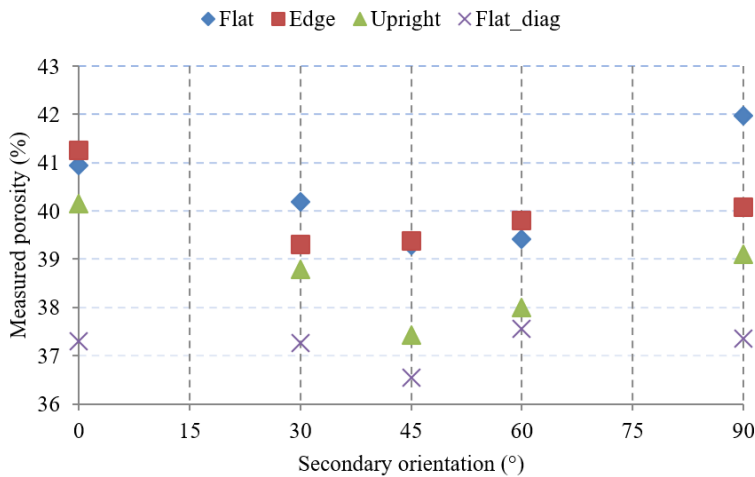


Fig. 7. Average measured porosity for various orientations

We can see that average porosity of specimens printed along Flat and Edge orientations is comparatively higher than other primary orientations. Similar results for Flat and Edge orientations are due to identical printing conditions for the cuboid shaped specimen. Porosity is lowest for Flat\_diag orientation. Rough surface and uneven profile of the pores is bound to occur due to inherent nature of the powder bed process. Relatively higher number of layers is needed to print specimen along Flat\_diag and Upright orientations. More number of layers introduces more inaccuracy in cylindricity of the pores. The lowest porosity for Flat\_diag orientation may be attributed to slant orientation of the specimens making axes of pores slant to the layer being printed. In this case, staircase effect comes into picture, as shown in Fig. 8.

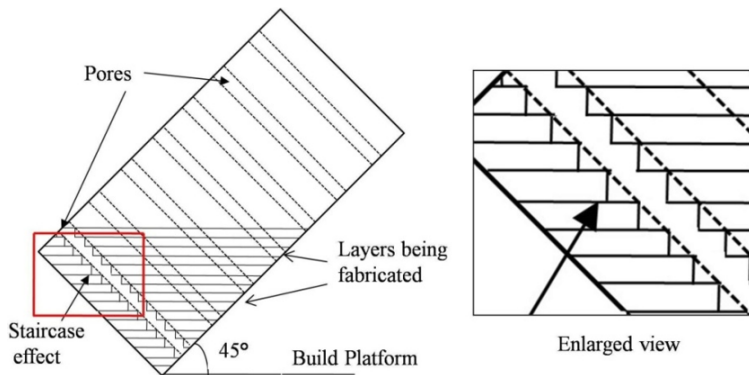


Fig. 8. Mechanism of layer deposition in Flat\_diag orientation  
 (Picture only for representation and not to scale)

The bar chart depicted in Fig. 9 shows percentage reduction from designed to measured porosities for various orientations. It is clear that relatively low reduction is obtained in the case of Flat/Edge orientations.

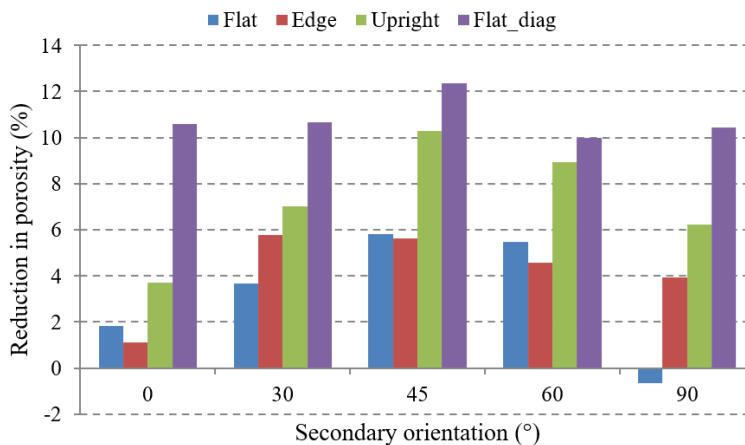


Fig. 9. Reduction in porosity for various orientations

### 3.3. Mechanical properties

Tensile, compression and impact testing were conducted to assess the mechanical behaviour of the fabricated porous specimens. Tensile test was performed using a porous dog-bone specimen, shown in Fig. 1a. The individual as well as average tensile strength (ultimate) with one SD for various primary and secondary orientations is provided in Table 2.

Table 2. Individual and average tensile strength (MPa) for various orientations

Primary orientation	Specimen no.	Secondary orientation				
		0°	30°	45°	60°	90°
Flat	S1	17.24	14.73	16.3	16.32	16.22
	S2	16.82	15.85	14.8	15.62	17.14
	S3	16.45	13.96	16.1	14.96	15.42
	Avg ± SD	16.84 ± 0.4	14.85 ± 0.95	15.73 ± 0.81	15.63 ± 0.68	16.26 ± 0.86
Edge	S1	14.78	15.12	13.56	14.32	15.24
	S2	14.23	13.68	14.63	12.62	13.45
	S3	15.37	13.84	14.84	13.74	13.92
	Avg ± SD	14.79 ± 0.57	14.21 ± 0.79	14.34 ± 0.69	13.56 ± 0.86	14.20 ± 0.93
Upright	S1	11.24	10.74	10.2	9.62	10.356
	S2	9.84	8.56	10.85	7.92	10.43
	S3	9.96	8.78	9.18	10.12	12.37
	Avg ± SD	10.35 ± 0.78	9.36 ± 1.20	10.08 ± 0.84	9.22 ± 1.15	11.05 ± 1.14
Flat_diag	S1	12.87	10.68	10.55	10.67	11.2
	S2	11.35	11.85	14.22	12.74	13.7
	S3	12.25	12.36	12.43	13.53	12.3
	Avg ± SD	12.16 ± 0.76	11.63 ± 0.86	12.40 ± 1.84	12.31 ± 1.48	12.40 ± 1.25

Table 2 reveals that tensile strength of the individual specimens printed along Flat orientation is comparatively higher than all other orientations. Tensile strength is lowest for the specimens printed along Upright orientation. This may be understood by the way printing takes place in different orientations. For specimens printed along Flat orientation, cross-section of the layers and layers' orientation remain along the tensile loading. Hence, greater load is needed to break the bond between layers. On the other hand, specimens printed in Upright and Flat\_diag orientations have relatively small cross-section; moreover, tensile loading is perpendicular to the layers. Hence, a smaller tensile load is required to break the bond between two adjacent layers. It is also noteworthy that SD for specimens printed along 0° orientations is lowest for a particular primary orientation. Stress-Strain diagram of specimens for 0° orientation is shown in Fig. 10.

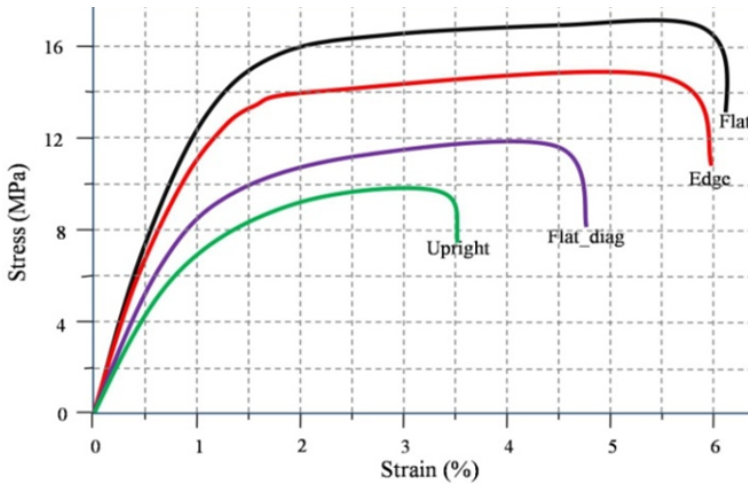


Fig. 10. Stress-strain diagram for specimens fabricated along  $0^\circ$  orientation

To visualise, interpret and compare the effect of orientations on tensile strength, results are plotted in Fig. 11. It can be seen that tensile strength of the specimens printed along Flat orientation is the highest; slightly lower for Edge orientation and the lowest for Upright orientation for all the secondary orientations. It is also interesting to see that relatively higher tensile strength is obtained for specimens printed along  $0^\circ$  orientation for all the primary orientations.

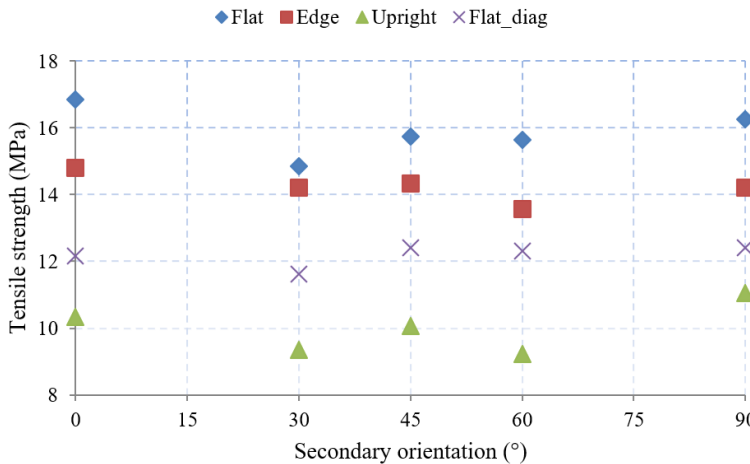


Fig. 11. Average tensile strength for various build orientations

Individual and average Young's moduli along with one SD for all the specimens have been summarised in Table 3.

As can be seen from the Fig. 12, the highest values of average Young's modulus are obtained for specimens printed along Flat orientation; average values ranging

Table 3. Individual and average Young's modulus (MPa) for various orientations

Primary orientation	Specimen no.	Secondary orientation				
		0°	30°	45°	60°	90°
Flat	S1	727	689	724	755	714
	S2	809	769	792	782	689
	S3	688	724	682	636	785
	Avg±SD	741.33±61.76	727.33±40.10	732.67±55.51	724.33±77.68	729.33±49.80
Edge	S1	720	649	735	695	765
	S2	748	688	658	715	675
	S3	698	724	692	642	710
	Avg±SD	722.00±25.06	687±37.51	695±38.59	684±37.72	716.67±45.37
Upright	S1	720	585	626	672	624
	S2	634	662	705	712	653
	S3	672	665	613	628	737
	Avg±SD	675.33±43.10	637.33±45.35	648.00±49.79	670.67±42.02	671.33±58.69
Flat_diag	S1	745	713	746	658	633
	S2	643	682	715	696	726
	S3	718	665	617	598	764
	Avg±SD	702.00±52.85	686.67±24.34	692.67±67.34	650.67±49.41	707.67±67.40

from 724 to 741 MPa for various secondary orientations. Here again, the lowest values are obtained for Upright orientations. This indicates that specimens printed along Flat orientation are stiffer and resistant to deformation in elastic range.

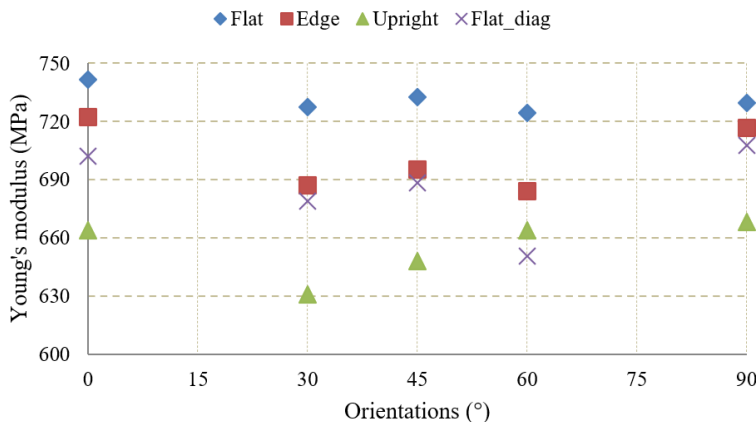


Fig. 12. Average Young's modulus for various build orientations

Compressive strength of the porous scaffold is very crucial for both load and non-load bearing cases. For load bearing cases, the scaffold must be able to withstand the load and should not collapse until tissues proliferate and support

the scaffold. For non-load bearing and *in-vitro* applications, the scaffold must possess adequate strength so that it does not break or collapse under the pressure exerted by sprouting cells. To analyse the behaviour of the porous scaffold under compression, a cuboid shaped specimen was used. The individual and average compressive strength values along with one SD have been summarised in Table 4. The compressive strength of various specimens ranges from 4.82 to 8.94 MPa.

Table 4. Individual and average compressive strength (MPa) for various orientations

Primary orientation	Specimen no.	Secondary orientation				
		0°	30°	45°	60°	90°
Flat	S1	7.85	6.57	6.92	7.68	8.16
	S2	6.92	7.16	7.12	6.34	7.26
	S3	7.9	7.68	7.43	8.12	6.64
	Avg±SD	7.56±0.55	7.14±0.56	7.16±0.26	7.38±0.93	7.35±0.76
Edge	S1	7.45	6.44	7.28	6.85	8.14
	S2	6.38	8.22	6.9	7.15	6.75
	S3	8.12	6.98	8.22	6.73	7.74
	Avg±SD	7.32±0.88	7.21±0.91	7.47±0.68	6.91±0.22	7.54±0.72
Upright	S1	7.85	7.65	7.67	7.98	8.52
	S2	8.66	7.78	8.12	7.32	8.94
	S3	8.1	8.42	7.26	8.18	7.32
	Avg±SD	8.20±0.41	7.95±0.41	7.68±0.43	7.83±0.45	8.26±0.84
Flat_diag	S1	6.23	5.11	6.85	4.82	6.78
	S2	5.23	4.87	5.46	5.86	6.45
	S3	6.34	5.72	5.24	5.46	5.65
	Avg±SD	5.93±0.61	5.23±0.44	5.85±0.87	5.38±0.52	6.29±0.58

Average compressive strength for various orientations has been presented in Fig. 13. From this figure, it is clearly visible that specimens printed along Upright orientation are superior in comparison with Flat and Edge orientations. It may be because of more number of layers printed in Upright orientation; moreover, layers are stacked parallel to loading direction, leading to more compressive load requirement for breaking the specimen. It is also interesting to see that compressive strengths of specimens printed along Flat and Edge orientation are very close to each other. It is due to cuboid shaped specimen. For specimens printed along Flat\_diag orientation, the layers remain 45° inclined to loading direction and fail easily, leading to low compressive strength.

Impact strength of the porous specimens has also been analysed. The Izod impact strength (J/m) for individual specimens is given in Table 5. The highest individual impact strength is recorded for Flat\_90° orientation; whereas the lowest individual impact strength is recorded for Upright\_30°. From Fig. 14, we can

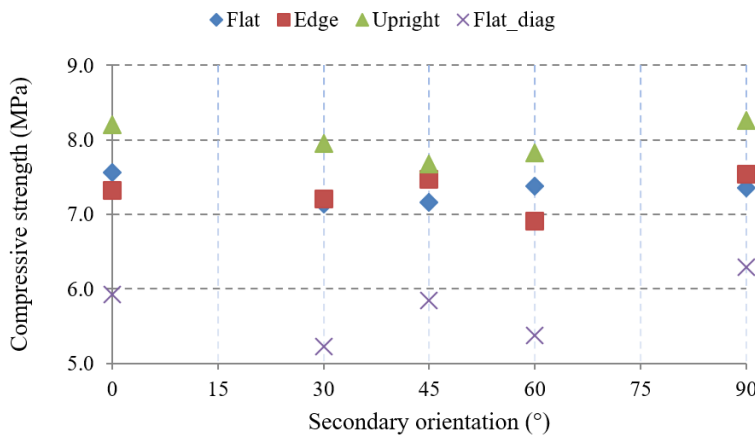


Fig. 13. Average compressive strength for various build orientations

see that the highest average impact strength is obtained for Flat<sub>0°</sub> orientation. It is evident that relatively better impact strength is obtained for Flat orientation. For Flat<sub>diag</sub> orientation, impact strength is not inferior to Flat and Edge orientation. Upright orientation provides the worst impact strength for all the secondary orientations.

Table 5. Individual and average Izod impact strength (J/m) for various orientations

Primary orientation	Specimen no.	Secondary orientation				
		0°	30°	45°	60°	90°
Flat	1	76.84	74.52	74.36	74.16	76.35
	2	77.32	75.44	73.24	72.47	77.54
	3	75.94	76.86	72.64	73.48	75.22
	Avg±SD	76.70±0.7	75.61±1.18	73.41±0.87	73.37±0.85	76.37±1.16
Edge	1	73.46	74.44	74.56	70.64	75.43
	2	74.62	72.28	72.34	72.62	72.85
	3	74.28	73.14	73.14	72.18	74.43
	Avg±SD	74.12±0.60	73.29±1.09	73.35±1.12	71.81±1.04	74.24±1.30
Upright	1	69.58	63.47	65.36	66.38	70.64
	2	68.48	69.73	68.24	69.48	71.58
	3	65.85	65.82	68.88	65.42	64.24
	Avg±SD	67.97±1.92	66.34±3.16	67.49±1.88	67.09±2.12	68.82±3.99
Flat <sub>diag</sub>	1	72.86	72.92	69.54	72.28	73.58
	2	73.58	70.23	72.72	73.54	73.48
	3	74.28	73.14	70.82	71.44	72.82
	Avg±SD	73.57±0.71	72.1±1.62	71.03±1.60	72.42±1.06	73.29±0.41

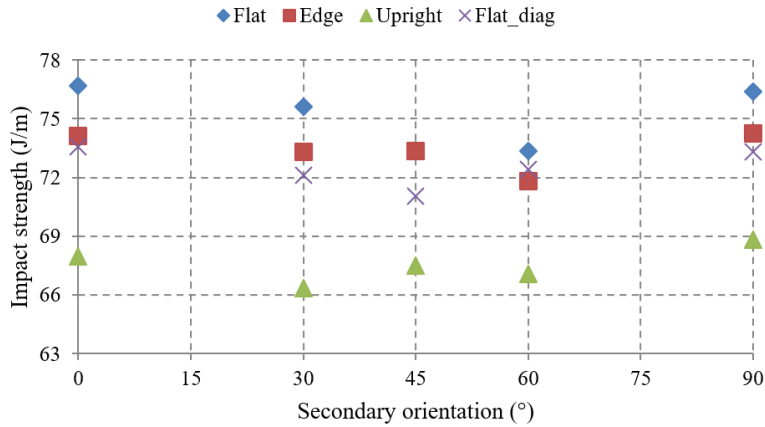


Fig. 14. Average impact strength for various build orientations

### 3.4. Dimensional analysis

To analyse the effect of build orientation on linear dimensions, we selected the length (25.4 mm) of the compression test specimen, shown in Fig. 1b. The length of each specimen for various orientations is measured. The average of three specimens along with one standard deviation (SD) is calculated and shown for each orientation angle in Table 6. From Table 6, we find that the lengths of specimens

Table 6. Individual and average length (mm) of the specimens for various orientations

Primary orientation	Specimen no.	Secondary orientation				
		0°	30°	45°	60°	90°
Flat	S1	25.42	25.4	25.41	25.37	25.39
	S2	25.39	25.36	25.42	25.42	25.37
	S3	25.38	25.39	25.4	25.38	25.4
	Avg±SD	25.40±0.02	25.38±0.02	25.41±0.01	25.39±0.03	25.39±0.02
Edge	S1	25.4	25.44	25.36	25.35	25.4
	S2	25.36	25.36	25.39	25.37	25.38
	S3	25.42	25.4	25.41	25.43	25.37
	Avg±SD	25.39±0.03	25.40±0.04	25.39±0.03	25.38±0.04	25.38±0.02
Upright	S1	25.46	25.4	25.41	25.42	25.38
	S2	25.41	25.47	25.49	25.4	25.43
	S3	25.38	25.39	25.48	25.51	25.49
	Avg±SD	25.42±0.04	25.42±0.04	25.46±0.04	25.44±0.06	25.43±0.06
Flat_diag	S1	25.37	25.42	25.49	25.45	25.42
	S2	25.48	25.45	25.42	25.5	25.38
	S3	25.46	25.43	25.39	25.41	25.45
	Avg±SD	25.44±0.06	25.43±0.02	25.43±0.05	25.45±0.05	25.42±0.04

fabricated in Flat and Edge orientations are significantly close to each other and their SD ranges between 0.01 to 0.04 mm. On the other hand, individual values in Upright and Flat\_diag orientation are relatively distinct from each other and show a relatively higher SD. This variation in dimensions can be understood considering the printing pattern of the specimens in different orientations. The overall length in Flat/Edge orientation is not affected by the number of layers deposited; whereas it is highly affected in Upright/Flat\_diag orientation. The cumulative thickness of all the layers gives the overall length in the case of Upright orientation, which leads to more chances of larger deviation in comparison with Flat orientation.

From Fig. 15, it is clear that the average length values of specimens fabricated along Flat/Edge orientation show much closeness to nominal value (25.4 mm). Flat and Edge orientations are identical in this case due to cuboid shaped specimen. On the other hand, specimens printed along Upright and Flat\_diag orientation possess lengths greater than the nominal value and their values range between 25.42 to 25.46 mm. Deviation in length values is the highest in the case of Upright orientation, which ranges between 0.04 to 0.06 mm. Moreover, lengths of all the specimens fabricated along Upright and Flat\_diag orientations are higher than nominal value at least by 0.02 mm. Individual values of the length varies from 25.36 to 25.51 mm, which gives max. deviation 0.15 mm, which is well within the tolerance suggested by the surgeon, approx. 0.5 mm for maxillofacial surgeries [40, 41]. It is interesting to note that SDs for the specimens printed along Flat and Edge orientations are relatively smaller than CDs of specimens printed along Upright and Flat\_diag orientations. It indicates that specimens printed along Flat and Edge orientations are consistent and close to the mean value.

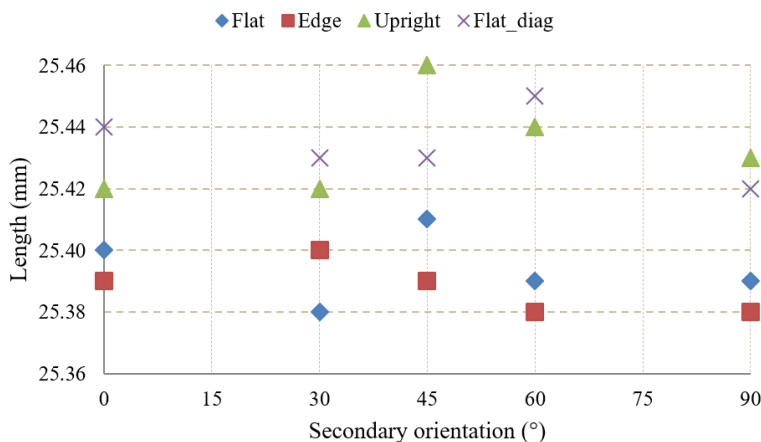


Fig. 15. Average length for various build orientations

The results of the current study are in line with the results obtained by previous researchers through their studies. For example, Stoia et al. [33] observed best tensile properties for selective laser sintered PA2200 samples printed along 0° and 90°

orientations in comparison with other orientations similar to the present study. Calignano et al. [42] also studied tensile behaviour of selective laser sintered PA12 parts at different orientations. They observed relatively higher tensile strength for Flat and Edge orientation; moreover, strengths along x- and y-axis were very close to each other. In this study also, we observed similar trends for tensile strength and tensile modulus. Stoia et al. [43] tested impact properties of laser-sintered polyamide PA2200 on various orientations. They obtained better impact strength (Charpy) for Flat and Edge orientation; whereas, the lowest impact strength for vertical orientation, which was similar to the present study. However, they reported the highest impact strength for Edge orientation; whereas, the present study revealed the highest strength for Flat orientation. Tomanik et al. [44] studied the effect of part orientation on mechanical properties of PA12 part fabricated on a desktop SLS system. They obtained the best tensile properties for parts printed along  $0^\circ$ , which is quite similar to the present study. However, they found part orientation to be insignificant for compression properties that is not the case of the present study.

#### 4. Conclusions

A comprehensive experimental study was performed to analyse the influence of part orientation inside the build chamber on selective laser sintered polyamide porous specimens mimicking the porous bone scaffolds. A good balance of porosity and mechanical strength in fabricated scaffold is vital for the success of tissue engineering process. In this work, a systematic study was carried out to assess the effect of part orientation on macro porosity, mechanical strength and dimensional accuracy of the porous polyamide specimens. Four primary (Flat, Edge, Upright and Flat\_diag) and five secondary ( $0^\circ$ ,  $30^\circ$ ,  $45^\circ$ ,  $60^\circ$ ,  $90^\circ$ ) orientations were considered to cover all the possible part orientations. Results confirm that part orientation has a significant influence on measured macro porosity, mechanical strength and dimensional accuracy of the fabricated porous specimens. The following conclusions have been drawn:

- Measured macro porosity of the specimens for all the orientations was found lower than the designed porosity. The best porosity was obtained for Flat\_90° orientation. In general, specimens printed along Flat/Edge orientation have shown better closeness to the designed porosity.
- Higher tensile strength was observed for porous specimens printed along Flat orientation. Maximum average tensile strength (16.84 MPa) was obtained for Flat\_0° orientation; whereas, minimum (9.22 MPa) obtained for Upright\_60° orientation.
- Specimens printed along Upright orientation have shown better compressive strength in general. Maximum average compressive strength (8.26 MPa) obtained for Upright\_90° orientation and minimum (5.23 MPa) obtained for Flat\_diag\_30° orientations.

- Relatively better average impact strength was obtained for specimens printed along Flat orientation. The highest average impact strength (76.70 MPa) was recorded for Flat\_0° orientation; whereas the lowest average impact strength (66.34 MPa) was recorded for Upright\_30°. Upright orientation provided the worst impact strength for all the secondary orientations.
- For dimensional accuracy, Flat orientation was found to provide the length closest to nominal value in comparison with other primary orientation.
- It is concluded that build orientation has a significant influence on porosity, strength and dimensional accuracy of the fabricated porous polyamide specimens. Careful selection of the primary and secondary build orientations may result in optimal values of the scaffold parameters.

### Acknowledgements

Authors are thankful to IISER, Bhopal and CIPET, Bhopal for the help and support extended during testing of the specimens.

### References

- [1] A. Kołakowska, A. Gadomska-Gajadur, and P. Ruśkowski. Biomimetic scaffolds based on chitosan in bone regeneration. A review. *Chemical and Process Engineering*, 43(3):305–330, 2022. doi: [10.24425/cpe.2022.142277](https://doi.org/10.24425/cpe.2022.142277).
- [2] V. Chadayammuri, M. Hake, and C. Mauffrey. Innovative strategies for the management of long bone infection: a review of the Masquelet technique. *Patient Safety in Surgery*, 9:32, 2015. doi: [10.1186/s13037-015-0079-0](https://doi.org/10.1186/s13037-015-0079-0).
- [3] J. Hu, J.H. Wang, R. Wang, X.B. Yu, Y. Liu and, D.A. Baur. Analysis of biomechanical behavior of 3D printed mandibular graft with porous scaffold structure designed by topological optimization. *3D Printing in Medicine*, 5:5, 2019. doi: [10.1186/s41205-019-0042-2](https://doi.org/10.1186/s41205-019-0042-2).
- [4] K.K. Sahu and Y.K. Modi. Investigation on dimensional accuracy, compressive strength and measured porosity of additively manufactured calcium sulphate porous bone scaffolds. *Materials Technology*, 36(8):492–503, 2021. doi: [10.1080/10667857.2020.1774728](https://doi.org/10.1080/10667857.2020.1774728).
- [5] Y.K. Modi and K.K. Sahu. Process parameter optimization for porosity and compressive strength of calcium sulfate based 3D printed porous bone scaffolds. *Rapid Prototyping Journal*, 27(2):245–255, 2021. doi: [10.1108/RPJ-04-2020-0083](https://doi.org/10.1108/RPJ-04-2020-0083).
- [6] H. Qu, H. Fu, Z. Han, and Y. Sun. Biomaterials for bone tissue engineering scaffolds: a review. *RSC Advances*, 9(45):26252–26262, 2019. doi: [10.1039/C9RA05214C](https://doi.org/10.1039/C9RA05214C).
- [7] C. Garot, G. Bettega, and C. Picart. Additive manufacturing of material scaffolds for bone regeneration: toward application in the clinics. *Advanced Functional Materials*, 31(5):2006967, 2021. doi: [10.1002/adfm.202006967](https://doi.org/10.1002/adfm.202006967).
- [8] B. Ostrowska, J. Jaroszewicz, E. Zaczyńska, W. Tomaszewski, W. Swieszkowski, and K.J. Kurzydłowski. Evaluation of 3D hybrid microfiber/nanofiber scaffolds for bone tissue engineering. *Bulletin of the Polish Academy of Sciences. Technical Sciences*, 62(3):551–556, 2014. doi: [10.2478/bpasts-2014-0059](https://doi.org/10.2478/bpasts-2014-0059).
- [9] S. Bose, S. Vahabzadeh, and A. Bandyopadhyay. Bone tissue engineering using 3D printing. *Materials Today*, 16(12):496–504, 2013. doi: [10.1016/j.mattod.2013.11.017](https://doi.org/10.1016/j.mattod.2013.11.017).

- [10] A. Eltom, G. Zhong, and A. Muhammad. Scaffold techniques and designs in tissue engineering functions and purposes: A review. *Advances in Materials Science and Engineering*, 2019:3429527, 2019. doi: [10.1155/2019/3429527](https://doi.org/10.1155/2019/3429527).
- [11] A. El Magri, S. Vaudreuil, K. El Mabrouk, and M. Ebn Touhami. Printing temperature effects on the structural and mechanical performances of 3D printed Poly-(phenylene sulfide) material. *IOP Conference Series: Materials Science and Engineering*, 783:012001, 2020. doi: [10.1088/1757-899X/783/1/012001](https://doi.org/10.1088/1757-899X/783/1/012001).
- [12] A. Dąbrowska-Tkaczyk, A. Floriańczyk, R. Grygoruk, K. Skalski, and P. Borkowski. Virtual and material models of human thoracic-lumbar spine with compressive fracture based on patients' CT data and the rapid prototyping technique. *Archive of Mechanical Engineering*, 58(4):425–440, 2011. doi: [10.2478/v10180-011-0026-2](https://doi.org/10.2478/v10180-011-0026-2).
- [13] K. Szlązak, J. Jaroszewicz, B. Ostrowska, T. Jaroszewicz, M. Nabiałek, M. Szota, and W. Swieszkowski. Characterization of three-dimensional printed composite scaffolds prepared with different fabrication methods. *Archives of Metallurgy and Materials*, 61(2):645–650, 2016. doi: [10.1515/amm-2016-0110](https://doi.org/10.1515/amm-2016-0110).
- [14] H.N. Singh, S. Agrawal, and Y.K. Modi. Additively manufactured patient specific implants: A review. *Archive of Mechanical Engineering*, 71(1):109–138. doi: [10.24425/ame.2024.149635](https://doi.org/10.24425/ame.2024.149635).
- [15] S. Zhang, S. Vijayavenkataraman, W. F. Lu, and J.Y. Fuh. A review on the use of computational methods to characterize, design, and optimize tissue engineering scaffolds with a potential in 3D printing fabrication. *Journal of Biomedical Materials Research Part B: Applied Biomaterials*, 107(5):1329–1351, 2019. doi: [10.1002/jbm.b.34226](https://doi.org/10.1002/jbm.b.34226).
- [16] C. Wang, W. Huang, Y. Zhou, L. He, Z. He, Z. Chen, X. He, S. Tian, J. Liao, B. Lu, and Y. Wei. 3D printing of bone tissue engineering scaffolds. *Bioactive Materials*, 5(1):82–91, 2020. doi: [10.1016/j.bioactmat.2020.01.004](https://doi.org/10.1016/j.bioactmat.2020.01.004).
- [17] P. Wang, Y. Sun, X. Shi, H. Shen, H. Ning, and H. Liu. 3D printing of tissue engineering scaffolds: a focus on vascular regeneration. *Bio-Design and Manufacturing*, 4(2):344–378, 2021. doi: [10.1007/s42242-020-00109-0](https://doi.org/10.1007/s42242-020-00109-0).
- [18] N. Przyszlak, A. Dulaska, T. Wróbel, and J. Szajnar. Grey cast iron locally reinforced using 3D printing scaffold insert. *Archives of Foundry Engineering*, 18(1):99–102, 2018. doi: [10.24425/118819](https://doi.org/10.24425/118819).
- [19] T. Kumaresan, R. Gandhinathan, M. Ramu, M. Ananthasubramanian, and K.B. Pradheepa. Design, analysis and fabrication of polyamide/hydroxyapatite porous structured scaffold using selective laser sintering method for bio-medical applications. *Journal of Mechanical Science and Technology*, 30:5305–5312, 2016. doi: [10.1007/s12206-016-1049-x](https://doi.org/10.1007/s12206-016-1049-x).
- [20] T. Alamro, M. Yunus, R. Alfattani, and I.A. Alnaser. Effect of part build orientations and sliding wear factors on tribological characteristics of FDM processed parts. *Archive of Mechanical Engineering*, 68(3):321–336, 2021. doi: [10.24425/ame.2021.138395](https://doi.org/10.24425/ame.2021.138395).
- [21] A. Korycki, C. Garnier, V. Nassiet, C.T. Sultan, and F. Chabert. Optimization of mechanical properties and manufacturing time through experimental and statistical analysis of process parameters in selective laser sintering. *Advances in Materials Science and Engineering*, 2022:2526281, 2022. doi: [10.1155/2022/2526281](https://doi.org/10.1155/2022/2526281).
- [22] G. Ziółkowski, E. Grochowska, D. Kęszycki, P. Gruber, V. Hoppe, P. Szymczyk-Ziółkowska, and T. Kurzynowski. Investigation of porosity behavior in SLSPolyamide-12 samples using X-ray computed tomography. *Materials Science-Poland*, 39(3):436–445, 2021. doi: [10.2478/msp-2021-0035](https://doi.org/10.2478/msp-2021-0035).
- [23] T. Kozior, M.M. Hanon, P. Zmarzły, D. Gogolewski, M. Rudnik, and W. Szot. Evaluation of the influence of technological parameters of selected 3D printing technologies on tribological properties. *3D Printing and Additive Manufacturing*, 2023. doi: [10.1089/3dp.2023.0080](https://doi.org/10.1089/3dp.2023.0080).

- [24] M.K. Razaviye, R.A. Tafti, and M. Khajehmohammadi. An investigation on mechanical properties of PA12 parts produced by a SLS 3D printer: an experimental approach. *CIRP Journal of Manufacturing Science and Technology*, 38:760–768, 2022. doi: [10.1016/j.cirpj.2022.06.016](https://doi.org/10.1016/j.cirpj.2022.06.016).
- [25] P.K. Jain, P.M. Pandey, and P.V. Rao. Experimental investigations for improving part strength in selective laser sintering. *Virtual and Physical Prototyping*, 3(3):177-188, 2008 .doi: [10.1080/17452750802065893](https://doi.org/10.1080/17452750802065893).
- [26] A. Pilipović, B. Valentan, and M. Šercer. Influence of SLS processing parameters according to the new mathematical model on flexural properties. *Rapid Prototyping Journal*, 22(2):258–268, 2016. doi: [10.1108/RPJ-08-2014-0092](https://doi.org/10.1108/RPJ-08-2014-0092).
- [27] J.P. Singh, P.M. Pandey, and A.K. Verma. Fabrication of three-dimensional open porous regular structure of PA-2200 for enhanced strength of scaffold using selective laser sintering. *Rapid Prototyping Journal*, 22(4):752–765, 2016. doi: [10.1108/RPJ-11-2014-0148](https://doi.org/10.1108/RPJ-11-2014-0148).
- [28] A.A. Mousa. Experimental investigations of curling phenomenon in selective laser sintering process. *Rapid Prototyping Journal*, 22(2):405–415, 2016. doi: [10.1108/RPJ-12-2013-0132](https://doi.org/10.1108/RPJ-12-2013-0132).
- [29] R.D. Goodridge, C.J. Tuck, and R.J.M. Hague. Laser sintering of polyamides and other polymers. *Progress in Materials Science*, 57(2):229–267, 2012. doi: [10.1016/j.pmatsci.2011.04.001](https://doi.org/10.1016/j.pmatsci.2011.04.001).
- [30] M. Yuan and D. Bourell. Orientation effects for laser sintered polyamide optically translucent parts. *Rapid Prototyping Journal*, 22(1):97-103, 2016. doi: [10.1108/RPJ-01-2014-0007](https://doi.org/10.1108/RPJ-01-2014-0007).
- [31] G.A. Adam and D. Zimmer. On design for additive manufacturing: evaluating geometrical limitations. *Rapid Prototyping Journal*, 21(6):662–670, 2015. doi: [10.1108/RPJ-06-2013-0060](https://doi.org/10.1108/RPJ-06-2013-0060).
- [32] G Berti, L D’angelo, A Gatto, and L. Iuliano. Mechanical characterisation of PA-AL2O3 composites obtained by selective laser sintering. *Rapid Prototyping Journal*, 16(2):124–129, 2010. doi: [10.1108/13552541011025843](https://doi.org/10.1108/13552541011025843).
- [33] D.I. Stoia, E. Linul, and L. Marsavina. Influence of manufacturing parameters on mechanical properties of porous materials by selective laser sintering. *Materials*, 12(6):871, 2019. doi: [10.3390/ma12060871](https://doi.org/10.3390/ma12060871).
- [34] L. Feng, Y. Wang, and Q. Wei. PA12 powder recycled from SLS for FDM. *Polymers*, 11(4):727, 2019. doi: [10.3390/polym11040727](https://doi.org/10.3390/polym11040727).
- [35] L. Zárbynická, J. Petrů, P. Krpec, and M. Pagáč. Effect of additives and print orientation on the properties of laser sintering-printed Polyamide 12 components. *Polymers*, 14(6):1172, 2022. doi: [10.3390/polym14061172](https://doi.org/10.3390/polym14061172).
- [36] A. El Magri, S.E. Bencaid, H.R. Vanaei, and S. Vaudreuil. Effects of laser power and hatch orientation on final properties of PA12 parts produced by selective laser sintering. *Polymers*, 14(17):3674, 2022. doi: [10.3390/polym14173674](https://doi.org/10.3390/polym14173674).
- [37] Product information PA2200, <https://www.eos.info/en/3d-printing-materials/plastic/polyamide-pa-12-alumide>. accessed on 26/09/2023.
- [38] Y. Zhang, N. Sun, M. Zhu, Q. Qiu, P. Zhao, C. Zheng, Q. Bai, Q. Zeng, and T. Lu. The contribution of pore size and porosity of 3D printed porous titanium scaffolds to osteogenesis. *Biomaterials Advances*, 133:112651, 2022. doi: [10.1016/j.msec.2022.112651](https://doi.org/10.1016/j.msec.2022.112651).
- [39] M. Schmid, A. Amado, and K. Wegener. Materials perspective of polymers for additive manufacturing with selective laser sintering. *Journal of Materials Research*, 29(17):1824–1832, 2014. doi: [10.1557/jmr.2014.138](https://doi.org/10.1557/jmr.2014.138).
- [40] A. Hills, K. Gowans, A. Di Biase, J. McKenzie, and N. Goodger. Accuracy of orthognathic surgery – a retrospective service evaluation. *International Journal of Oral and Maxillofacial Surgery*, 46:158, 2017. doi: [10.1016/j.ijom.2017.02.545](https://doi.org/10.1016/j.ijom.2017.02.545).
- [41] M. Mandolini, M. Caragiuli, A. Brunzini, A. Mazzoli, and M. Pagnoni. A procedure for designing custom-made implants for forehead augmentation in people suffering from Apert syndrome. *Journal of Medical Systems*, 44:146, 2020. doi: [10.1007/s10916-020-01611-9](https://doi.org/10.1007/s10916-020-01611-9).

- [42] F. Calignano, F. Giuffrida, and M. Galati. Effect of the build orientation on the mechanical performance of polymeric parts produced by multi jet fusion and selective laser sintering. *Journal of Manufacturing Processes*, 65:271–282, 2021. doi: [10.1016/j.jmapro.2021.03.018](https://doi.org/10.1016/j.jmapro.2021.03.018).
- [43] D.I. Stoia, S.V. Galatanu, and L. Marsavina. Impact properties of laser sintered polyamide, according to building orientation. *Journal of Mechanical Science and Technology*, 37(3):1119–1123, 2023. doi: [10.1007/s12206-022-2108-0](https://doi.org/10.1007/s12206-022-2108-0).
- [44] M. Tomanik, M. Żmudzińska, and M. Wojtków. Mechanical and structural evaluation of the PA12 desktop selective laser sintering printed parts regarding printing strategy. *3D Printing and Additive Manufacturing*, 8(4):271–279, 2021. doi: [10.1089/3dp.2020.0111](https://doi.org/10.1089/3dp.2020.0111).